NeuroImage 297 (2024) 120703

Contents lists available at ScienceDirect

NeuroImage

journal homepage: www.elsevier.com/locate/ynimg

Optimal navigability of weighted human brain connectomes in physical space

Laia Barjuan [a,b], Jordi Soriano [a,b], M. Ángeles Serrano [a,b,c,*]

[a] Departament de Física de la Matèria Condensada, Universitat de Barcelona, Martí i Franquès 1, E-08028 Barcelona, Spain
[b] Universitat de Barcelona Institute of Complex Systems (UBICS), Universitat de Barcelona, Martí i Franquès 1, E-08028, Barcelona, Spain
[c] ICREA, Pg. Lluís Companys 23, E-08010 Barcelona, Spain

ARTICLE INFO

Dataset link: https://doi.org/10.5281/zenodo.11198345, https://github.com/networkgeometry

Keywords:
Network neuroscience
Brain connectomes
Weighted structure
Spatial embedding
Navigability
Complex networks

ABSTRACT

Communication protocols in the brain connectome describe how to transfer information from one region to another. Typically, these protocols hinge on either the spatial distances between brain regions or the intensity of their connections. Yet, none of them combine both factors to achieve optimal efficiency. Here, we introduce a continuous spectrum of decentralized routing strategies that integrates link weights and the spatial embedding of connectomes to route signal transmission. We implemented the protocols on connectomes from individuals in two cohorts and on group-representative connectomes designed to capture weighted connectivity properties. We identified an intermediate domain of routing strategies, a *sweet spot*, where navigation achieves maximum communication efficiency at low transmission cost. This phenomenon is robust and independent of the particular configuration of weights. Our findings suggest an interplay between the intensity of neural connections and their topology and geometry that amplifies communicability, where weights play the role of noise in a stochastic resonance phenomenon. Such enhancement may support more effective responses to external and internal stimuli, underscoring the intricate diversity of brain functions.

1. Introduction

The architecture of the human brain has been evolutionary shaped in a three-dimensional Euclidean space to optimize specialization and adaptation to a changing environment (Stiso and Bassett, 2018; Bullmore and Sporns, 2012; Ercsey-Ravasz et al., 2013; Schwartz et al., 2023). As a result, communication processes in the brain are extremely efficient, enabling ultrafast responses to a diversity of external and internal stimuli. At the macroscopic level, the transfer of information in these communication processes is sustained by neural networks of white matter fibers that connect neurons across different brain regions, and whose wiring diagrams are conventionally termed connectomes (Sporns et al., 2005). Human connectomes are complex, and their structure is characterized by small worldness (Watts and Strogatz, 1998; Sporns et al., 2004; Bassett and Bullmore, 2006; He et al., 2007; Hagmann et al., 2007; Bassett and Bullmore, 2017), heterogeneous degree distributions (Gong et al., 2009; Gastner and Ódor, 2016), the rich-club effect (Van Den Heuvel and Sporns, 2011), and modularity (Sporns and Betzel, 2016; Meunier et al., 2010). These structural features influence decisively communication mechanisms and all our cognitive processes (Bressler and Menon, 2010; Deco and Kringelbach, 2014; Honey et al., 2007).

Understanding the intricacy of the human connectome and its impact on cognitive processes is a daunting task. However, when its topological organization is combined with its anatomical spatial embedding, the human connectome reveals itself as a comprehensive, highly useful map of the brain to understand large-scale neural communication. In recent years, modeling based on these maps in combination with geometric routing protocols have shed light on the informational cost associated with the selection of efficient routes in the brain (Seguin et al., 2018; Allard and Serrano, 2020; Cannistraci and Muscoloni, 2022; Seguin et al., 2023).

The most efficient routes would correspond to pathways with short topological path lengths that decrease conduction latency, minimize the impact of noise introduced by synaptic retransmission, and reduce metabolic costs (Avena-Koenigsberger et al., 2018), but their computation requires full knowledge of the connectome's topology. By contrast, a decentralized greedy routing dynamics on geometric maps of connectomes, guided by a local rule that sends information to the connected region closest in spatial distance to a target destination, has shown that brain networks are highly navigable (Seguin et al., 2018; Allard and Serrano, 2020), with an efficiency similar to topological shortest path

* Corresponding author.
E-mail address: marian.serrano@ub.edu (M.Á. Serrano).

https://doi.org/10.1016/j.neuroimage.2024.120703
Received 11 April 2024; Received in revised form 17 June 2024; Accepted 21 June 2024
Available online 25 June 2024

routing but without requiring information about all possible routes, a condition that is highly unlikely in a physiological system.

As an alternative to spatial distances, routing strategies can be guided by link weights (e.g., nerve fiber density) once these weights are transformed into weight distances such that higher weights correspond to shorter weight distances. In Avena-Koenigsberger et al. (2019), weight distances between connected brain regions were used to explore a continuous spectrum of stochastic protocols that interpolate between random-walk diffusion at one extreme, using only local information but performing inefficiently, and shortest path routing at the other, highly efficient but requiring full knowledge of the global weighted topology of the brain connectome. In between, a small increase in the bias towards global information progressively achieved improved efficiency at low informational cost.

In this work, we introduce a theoretical framework to investigate the interplay between spatial distances and link weights in communication processes between brain regions, and apply it to human connectomes reconstructed from empirical data. Our framework facilitates the characterization of the distinctive roles played by the *hard* and *soft wiring* of the brain. The former describes the topology of the connectome and the spatial distances in its geometric embedding, both shaped by evolutionary processes. The latter entails the weights of the links between connected brain regions, affected by plasticity and functional needs. More specifically, we applied a continuous spectrum of stochastic routing protocols, having the greedy routing strategy at one extreme and a weight-biased random walk at the other extreme, on two cohorts of real human connectome networks. These protocols overall account for the expectation that signals are more likely to travel through pathways with more nerve fibers and that nearby nodes are connected with higher probability. We found that there is an intermediate region in this spectrum, a *sweet spot*, in which connectomes become maximally navigable and achieve full communication efficiency. Additionally, in this region, weights, topology and spatial distances are coupled in such a way that information transmission is not only maximally efficient but also robust even under severe insult. Remarkably, this *sweet spot* is independent of the particular configuration of weights, suggesting that weights effectively act as noise, such as in stochastic resonance, and facilitate the exploration of new routes for optimal navigability.

2. Data and methods

2.1. Data description

Our study is based on two different datasets, comprising a total of 84 weighted connectomes of healthy human subjects.

The University of Lausanne (UL) dataset includes connectomes of 40 healthy subjects (16 females), approximately 25 years old, obtained from diffusion spectrum MRI images (DSI). The images were taken on a 3T Siemens Trio scanner with a 32-channel head coil, MPRAGE sequence of 1 mm in-plane resolution, and 1.2 mm slice thickness. The sequence included 128 diffusion weighted volumes and an extra b_0 volume, with $b_{\max} = 8000$ s/mm^2 and a voxel size of $2.2\times2.2\times3.0$ mm^3. EPI sequence was 3.3 mm for both in-plane resolution and thickness, with TR = 1920 ms. To track neural fibers connecting pairs of regions, whole-brain deterministic streamline tractography was performed on reconstructed DSI data, initiating 32 streamline propagations (seeds) per diffusion direction and white-matter voxel by following directions of maximum diffusion. Within each voxel, seeds were randomly placed, and for each seed, a fiber streamline was grown in two opposite directions with a 1 mm fixed step. Fibers were stopped whenever a change in direction was greater than 60 degrees/mm. The process was completed when both ends of the fiber left the white-matter mask. The data was processed using The Connectome Mapper Toolkit (Tourbier et al., 2020).

The Human Connectome Project (HCP) dataset (Van Essen et al., 2012) was used for cross-validation. It consists of 44 connectomes (31 females), aged between 22 and 35 years, obtained from T1-weighted and corrected diffusion-weighted magnetic resonance images (DWIs). The data was collected for shells $b = 1000, 2000$ and 3000 s/mm^2 and 270 directions in total, with a voxel size of $1.25 \times 1.25 \times 1.25$ mm^3. The already preprocessed (Glasser et al., 2013) DWI data of each subject was employed to fit a second-order tensor for each voxel and its different voxelwise scalar maps by using Dipy (Garyfallidis et al., 2014). The DWIs were also used to estimate the intravoxel fODF by using the Constrained Spherical Deconvolution (Tournier et al., 2007) approach implemented in MRtrix3 (https://www.mrtrix.org/), which applies high-angular resolution to estimate the orientation of multiple intravoxel fiber populations within regions of complex white-matter architecture. This fODFs were used by the SDSTREAM deterministic fiber-tracking algorithm (Tournier et al., 2012) to obtain the streamlines distribution for each subject.

For the two datasets, the structural connectivity matrices between Regions of Interest (ROIs), encompassing both hemispheres, were computed defining the intensities of connections between each pair of regions as the density of streamlines connecting them. The cortex's parcellation was defined at five different resolutions using a fine-graining process applied to the 83 ROIs defined by the Desikan–Killiany atlas, as described in Cammoun et al. (2012). In this work, we used the high-resolution parcellation of the multiscale reconstruction comprising $N = 1015$ ROIs (including the brainstem).

2.2. Definitions of weight, strength, and distances

We measured the weight of a link between a connected pair of ROIs as the fiber density of white matter tracts, i.e., the number of streamlines connecting the two brain regions per unit surface, where each streamline is corrected by its average length in millimeters. The aim of these normalizations is to control for the variability in cortical region size and the linear bias toward longer streamlines introduced by tractography algorithms. More specifically, the weight w_{ij} of the connection between ROIs i and j was calculated as

$$w_{ij} = \frac{2}{A_i + A_j} \sum_{f \in F_e} \frac{1}{l(f)}, \tag{1}$$

where A_i and A_j are the areas of ROIs i and j respectively, F_e is the set of all fibers connecting ROIs i and j, and $l(f)$ is the length of the fiber. The sum of all weights incident to a ROI i define its strength s_i. If k_i is the degree of ROI i, meaning that it is connected to k_i other regions, the strength of node i is calculated as $s_i = \sum_{j=1}^{k_i} w_{ij}$.

Finally, we used the coordinates of the centers of the ROIs in the 3D Euclidean space to compute spatial distances between regions, measured in millimeters. To investigate their interplay with links' weights, we transformed weights into weight distances by interpreting them as a proximity measure, such that big weights are transformed into small weight distances and small weights into big weight distances. We used the proximity-to-distance mapping from Avena-Koenigsberger et al. (2019), used also in Goñi et al. (2014) and Avena-Koenigsberger et al. (2017), and defined as

$$d_{ij} = A \ln(1/w_{ij}), \tag{2}$$

where d_{ij} is the weight distance corresponding to the weight w_{ij}, and the parameter $A = 1$ mm is introduced to ensure correct dimensionality.

To smooth out the intrinsic noisy behavior of the aforementioned magnitudes, a common practice in network science consists in averaging over degree classes or spatial bins, depending on the metric. As a result, the averages obtained display more clearly the tendency of the data such that the fittings are more reliable. This averaging technique will be used in the analysis of the data in the Results section.

2.3. Disparity of weights

The organization of weights in the connectome can be characterized at the global scale by their statistical distribution and by the distribution of strengths. At the local level, the disparity function (Serrano et al., 2009) measures the variability in the weights w_{ij} of the connections attached to a ROI i. Its expression is given by

$$Y(k_i) \equiv k_i Y(k_i) = k_i \sum_{j=1}^{k_i} p_{ij}^2 = k_i \sum_{j=1}^{k_i} (w_{ij}/s_i)^2, \tag{3}$$

where the region has degree k_i and strength s_i. $Y(k_i) = 1$ whenever the strength of the region is distributed homogeneously between its connections, and $Y(k_i) = k_i$ whenever just one link accumulates all the strength.

We note that when $Y(k_i) < \mu(Y_{\text{null}}(k_i)) + a\sigma(Y_{\text{null}}(k_i))$, where the average μ and the variance σ^2 are

$$\mu(Y_{\text{null}}(k_i)) = \frac{2k_i}{k_i + 1} \tag{4}$$

and

$$\sigma^2(Y_{\text{null}}(k_i)) = k_i^2 \left(\frac{20 + 4k_i}{(k_i + 1)(k_i + 2)(k_i + 3)} - \frac{4}{(k_i + 1)^2} \right), \tag{5}$$

then the disparity is consistent with the null hypothesis that the normalized weights w_{ij}/s_i are uniformly distributed at random. The variable a is a constant determining the confidence interval. The larger a is, the more restrictive the null model becomes and the more disordered weights should be for local heterogeneity to be detected. In this study we use the typical value $a = 2$.

2.4. Group-representative connectome

Group-representative connectomes can be constructed to disregard subject-to-subject fluctuations. In this work, we constructed a group-representative weighted connectome for each dataset using the distance-dependent consensus threshold method described in Mišić et al. (2015) and Betzel et al. (2019). First, all edges present in the individual subjects are binned according to their length. In our case we used 22 bins. In each bin we keep a certain number of the connections with bigger consensus across humans. The number of connections kept in each bin is calculated as the average across subjects of the number of connections that fit in that bin at the subject-level. For example, if the average number of connections across subjects in bin i is equal to n_i, we keep the n_i most commonly occurring edges in that bin. We carried out this process independently for inter- and intra-hemispheric connections to ensure that inter-hemispheric links are not systematically under-represented.

Typically, the weights of the connections in group-representatives are computed using the averaging method (Van Den Heuvel and Sporns, 2011; Goñi et al., 2014; Seguin et al., 2018), which consists in assigning the weight of a connection by averaging over all weights in the dataset related to that connection. However, we have seen that this approach destroys some of the weighted properties of the connectomes. To overcome this limitation, we implemented a different approach in which, to assign a weight to a connection, we selected at random one weight from all weights in the dataset related to that connection. Different realizations of this selection process gave similar results. This group-representative not only preserves the topological features of the original connectomes but also the properties of the distributions of weights and strengths, and we have termed it the distance-dependent weighted (DDW) group-representative.

2.5. Greedy routing protocol

In the standard deterministic greedy routing protocol (Kleinberg, 2000; Allard and Serrano, 2020), a signal navigates the brain to reach a destination node from a source node by selecting as a transient stop the neighbor connected to the source with the minimum spatial distance to the destination, from where the process is repeated. In this strategy, each node only requires information about their connected neighbors and their distances to the final destination, which can be easily calculated from the coordinates in the embedding space. This makes greedy routing a distributed strategy much more computationally efficient as compared to routing through topological shortest paths. However, signals may get trapped in a loop and fail to reach the destination.

In the stochastic version of the greedy routing protocol, there is a probability that the signal travels from node i to any connected neighbor j in its way to the final target z, which is inversely proportional to the distance from the neighbor to the target. In this version, signals eventually reach the destination, but they may take an exceedingly large time. Therefore, a time-out should be introduced to disregard extremely long times (Ortiz et al., 2017).

2.6. Weight-biased random walk

A weight-biased random walk is a stochastic process in which a signal travels from a source region to one of its neighbors with a probability that is proportional to the weight of their connection. In other words, a signal in region i will travel to the neighboring region j with probability $P(j|i) = w_{ij}/s_i$, where w_{ij} is the weight of their connection, and s_i corresponds to the strength of region i.

Using a weight-biased random walk to diffuse signals from a source to a target ensures that the signal will arrive. However, it can take very long detours before reaching its destination. Therefore, like in stochastic greedy routing, a time-out must be introduced to ignore exceedingly long walks.

2.7. Performance metrics

The performance of communication protocols in brain connectomes can be evaluated through two standard metrics widely employed to assess the efficiency of routing strategies in complex networks, namely, the success rate and the average stretch. The success rate is the fraction of paths that reach a ROI target successfully, considering all possible source/target pairs of ROIs in the connectome. On the other hand, the stretch of a successful path is calculated as the ratio between the number of links in the path and the number of links in the topological shortest path between source and target. The average stretch is computed over all successful paths.

Additionally, we calculated the average transmission cost introduced in Avena-Koenigsberger et al. (2019). The distance immediate transmission cost of a node i is the expected distance that a signal has to travel to move to a neighbor of i when going to the target z. The Euclidean distance immediate transmission cost and weight distance immediate transmission cost are computed as

$$c_E^{\text{trans}}(i, z) = \sum_j P(j \mid i, z) \cdot d_{ij}^{\text{E}} \tag{6}$$

and

$$c_w^{\text{trans}}(i, z) = \sum_j P(j \mid i, z) \cdot d_{ij}^{w}, \tag{7}$$

where j are the neighbors of node i, $P(j \mid i, z)$ is the probability of transition from node i to its neighbor j when going to node z, and d_{ij} is the distance from node i to its neighbor j.

The total transmission cost of a path is computed by adding the immediate transmission cost of all nodes visited through the path. Likewise, the total transmission cost in a network is calculated as the average transmission cost of all paths.

2.8. Null models of weighted brain connectomes

To assess the role of weights and spatial distances in the navigability properties of weighted human brain connectomes, we consider three null models.

- *Coordinate-Preserving Weight-Reshuffling (CP-WR),* which preserves the geometry and topology of the network, but reassigns the weights of the connections at random.
- *Coordinate-Preserving Weight-Detached (CP-WD),* which preserves the geometry and topology of the network, but disregards weights.
- *Coordinate-Reshuffling Weight-Preserving (CR-WP),* which preserves the topology and weights, but randomizes the geometry by re-assigning the position of the nodes in the Euclidean embedding space.

We found that there is very little variation between the results obtained from different realizations of the reshufflings, see Section 4.4. Therefore, we only carried out one realization per subject for each time-out.

2.9. Navigation resilience

We evaluated the resilience of information transfer under perturbations affecting the number of accessible ROIs in the group-representative connectome of the UL Dataset. The three methods used to damage the network were targeted attack on highest degree (HD), targeted attack on highest strength (HS) and random failure (RD). For the HD and HS targeted attacks, the ROIs deleted were the ones with highest degree and highest strength, respectively. For the random failure, the deleted ROIs were selected at random. Since random failure can give different results depending on the realization, we averaged the results over 10 realizations. We studied the effect of deleting from 1 to 900 ROIs of the network using intervals of 25, 50 or 100 ROIs. The validity of the group-representative was corroborated by the analysis of seven individuals in the UL dataset.

As an additional check on the resilience of the network, we computed the relative size of the giant connected component after the attacks. The giant connected component of a network is defined as the connected subgraph with the largest fraction of nodes in the network, and we used the `networkX` package to calculate it. Then, we divided the giant component size by the total number of nodes remaining in the network to obtain its relative size.

3. A model for navigating connectomes by weights and distances

The crucial methodological innovation in our study is the introduction of a communication protocol that combines a stochastic greedy routing and a weight-biased random walk, such that signals are preferentially sent along paths with larger connection weights and to regions closer to the target in the embedding space.

We define a family of routing models that we term 'high-weight short-distance' (HWSD) routing processes. In these processes, weight distances and physical distances are balanced according to a parameter λ. Namely, the transition probability from node i to its neighbor j when traveling to target z is

$$P_\lambda(j\ |i,z) = \exp\left[-(\lambda \cdot d^{\mathrm{E}}_{jz} + (1-\lambda)\cdot d^{w}_{ij})\right]\frac{1}{Z^z_i}, \tag{8}$$

where $Z^z_i = \sum_j \exp\left[-(\lambda \cdot d^{\mathrm{E}}_{jz} + (1-\lambda)\cdot d^{w}_{ij})\right]$ is a normalization factor, d^{E} is the Euclidean distance between the centers of the regions, and d^w is the distance obtained by transforming weights such that higher weights correspond to shorter weight distances. By gradually changing the value of $\lambda \in [0,1]$, the dynamics shifts from a weight-biased random walk at $\lambda = 0$, where the transmission is guided by local information provided by connection weights, to a pure stochastic greedy routing at $\lambda = 1$, where the dynamics is controlled by spatial distances, i.e. map navigation. Fig. 1 provides an illustrative scheme of the two extremes of the spectrum. We selected the set of λ values to run the simulation experiments by separating the navigation spectrum in two subintervals. We used a linear sampling of values of λ in the subinterval $[0.3, 1]$, while we used a logarithmic sampling in the subinterval $[0, 0.3]$ to explore a wider range of smaller parameter scales.

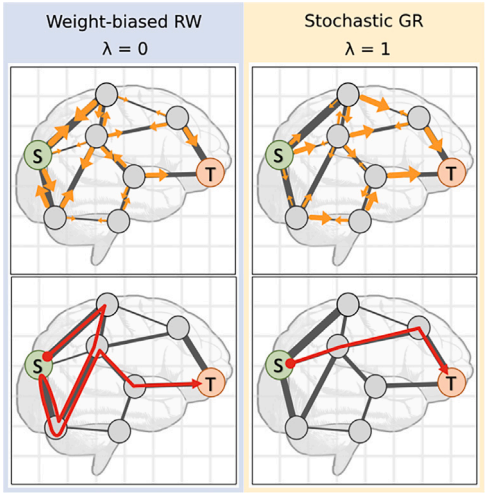

Fig. 1. Extreme cases of the navigation protocol. Top row: the probability of transition from one node to its neighbor is represented by an orange arrow. A bigger arrow corresponds to a larger probability. Bottom row: examples of a path taken by the signal in each case. The left column corresponds to the case where $\lambda = 0$, i.e. weight-biased random walk, and the right column to the case where $\lambda = 1$, i.e. stochastic greedy routing. The source node is depicted in green and the target node in orange.

The proposed procedure is probabilistic. Then, the signal eventually reaches the destination with certainty, in contrast to deterministic greedy routing in which some paths may encounter a halt. However, some instances, specially abundant in the weight-biased random walk side of the routing spectrum, could take an excessive number of steps. Thus, we applied a time-out (measured in maximum number of steps) after which we assumed that the signal faded out. We performed the navigation for time-out values of 1000, 2500, 5000, 10 000 and 30 000.

4. Results

We report summary statistics for all the individual connectomes and for the group-representatives of the UL and HCP datasets in Tables ST1 and ST2 of the Supplementary Material (SM). The tables include the number of nodes, number of edges, average degree, maximum degree, average weight, maximum weight, average strength, maximum strength, average shortest path, diameter of the network, mean average spatial distance to nearest neighboring regions, and mean maximum spatial distance to nearest neighboring regions.

Excluding the brainstem, the connectomes comprise $N = 1014$ ROIs with approximately equal surface area. There is a negligible variability in the number of nodes across subjects due to the removal of regions that were disconnected in the original dataset or that became disconnected after the removal of the brainstem, and of regions that were only connected to themselves by a self-loop. The connectomes in the two datasets are sparse, as expected from deterministic streamline tractography methods. The UL dataset has a lower mean of the average degree than the HCP dataset, with values 27.62 and 78.43, respectively. Likewise, the HCP dataset has almost three times more connections per connectome than the UL Dataset, and a maximum degree which is almost twice the one in the UL dataset. Consequently, its average diameter, which is the largest shortest path between nodes in the network, is smaller than the average diameter of the UL dataset. Since

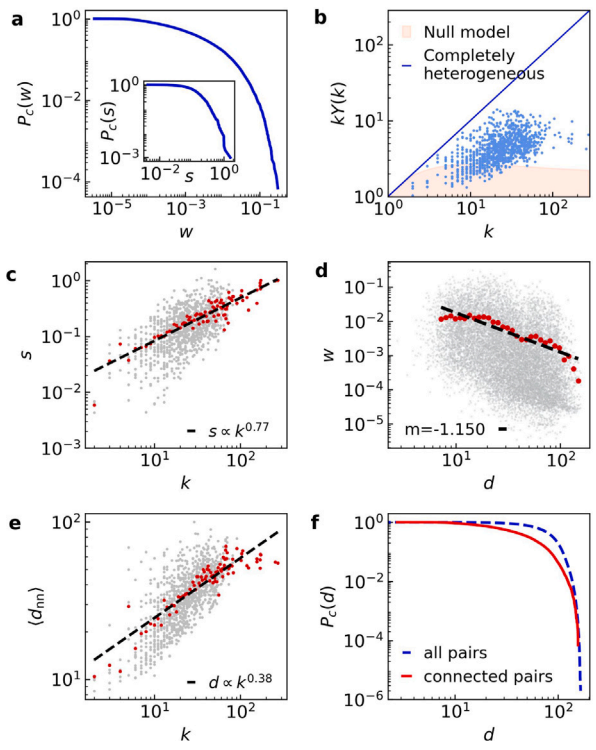

Fig. 2. Weights and distances in the connectome of subject 34 in the UL dataset. (a) Complementary cumulative weight distribution. Inset: complementary cumulative strength distribution. (b) Scattered plot of the disparity of weights. Each sky-blue dot corresponds to one ROI. The blue line represents the completely heterogeneous scenario, $k_i Y(k_i) = k_i$. Complete homogeneity corresponds to $k_i Y(k_i) = 1$. The orange area represents the region compatible with the null hypothesis, which assumes weights distributed uniformly at random. (c) Strength of ROIs versus their degree. Each gray dot corresponds to one ROI. The red dots are the average strength in every degree class. (d) Weight of links versus their associated spatial distance. Each gray dot corresponds to one link. The red dots are the average weight in 30 logarithmically spaced bins. (e) Average distance to connected neighboring regions versus degree of ROIs. Each gray dot corresponds to one ROI. The red dots are the average distance in every degree class. In (c), (d), and (e), the dashed line is a power-law fit of the averages represented by the red dots. (f) Complementary cumulative distance distribution. The dashed blue curve represents the distribution of distances between all pairs of ROIs and the solid red curve only between connected pairs.

the connectomes in the HCP dataset are more densely connected, it would be reasonable to expect slightly better navigation performance than in the UL dataset. These differences between the two datasets are attributable to acquisition parameters and are not influenced by biological sex. More details on the compatibility between the measures obtained for males and females can be found in Table ST3 of the SM.

4.1. Correlation between weights and spatial distances

The properties of weights and spatial distances of connections between brain regions in a typical subject in the UL dataset are shown in Fig. 2. Results for the rest of UL connectomes are reported in Supplementary Figs. SF1–SF7, and results for the connectomes in the HCP dataset are in Figs. SF48–SF54. In general, the results were consistent in the two cohorts and across subjects.

Fig. 2a features the complementary cumulative distribution of weights $P_c(w)$, which is highly heterogeneous and ranges over four orders of magnitude. Fig. 2b shows the local distribution of weights for each ROI as measured by the disparity $Y(k_i)$. This metric reveals that the total strength associated to brain regions is unevenly distributed between their connections and some of them concentrate significantly larger weights. The weight distribution and the local disparity are retained in the DDW group-representative, see Figs. SF11–SF12 and SF56. This is in contrast to the group-representative where weights are obtained with the averaging method, which provides more homogeneous weight distributions both at the global and at the local scale, as measured respectively by the complementary cumulative weight distribution and the disparity, see SF13. Finally, the complementary cumulative strength distribution $P_c(s)$, inset in Fig. 2a, displays a homogeneous region for low values of the strength and a tail that decays as a power-law with characteristic exponent close to -2.

The relation between strength and degree, $s(k)$, Fig. 2c, also exhibits a power-law behavior with average exponents $\langle \mu \rangle = 0.8 \pm 0.1$ and $\langle \mu \rangle = 0.71 \pm 0.07$ for subjects in the UL and HCP datasets, respectively. This is in stark contrast with complex networks in other domains, which typically display a superlinear relation. Hence, hubs in brain connectomes accumulate less strength than expected given their connectivity. This effect can be explained by two observations. First, as shown in Fig. 2e, higher degree nodes have a longer average distance to connected neighbors $\langle d_{nn} \rangle(k)$ than lower degree nodes, which tend to connect preferentially to closer neighbors. The average distance to connected neighbors increases as a power-law of the degree with positive average exponents $\langle \mu \rangle = 0.36 \pm 0.04$ and $\langle \mu \rangle = 0.281 \pm 0.019$ in the UL and HCP datasets, respectively. Second, the longer the distance between connected nodes, the smaller the weight of the connection between them, as proved by the power-law decay of the weight as a function of the spatial distance, $w(d) \approx d^{\mu}$ with average exponent $\langle \mu \rangle = -1.12 \pm 0.13$ for the UL Dataset, Fig. 2d and Fig. SF7, and $\langle \mu \rangle = -2.0 \pm 0.1$ for the HCP Dataset, shown in Fig. SF54.

Finally, the complementary cumulative distance distribution $P_c(d)$ between connected pairs of regions, shown in Fig. 2f, is slightly more heterogeneous than the distribution of distances between all regions in the connectome, although both are limited by the size of the brain.

4.2. Navigating human connectomes by weights and spatial distances

In the previous section, we provided evidence that the weights of the connections in human brain connectomes and the spatial distances that they cover are inversely correlated. It is then natural to study their interplay in navigation protocols that take into account both magnitudes. Fig. 3 shows the results obtained with our HWSD navigation protocol.[1] Specifically, Fig. 3a and b provide, respectively, the mean success rate and mean average stretch across the 40 subjects in the UL dataset. The results for the HCP dataset are reported in Fig. SF55. The spatial and weight distances transmission costs are shown in Figs. SF8 and SF55.[2]

In Fig. 3a and b we can see that pure stochastic greedy routing, corresponding to $\lambda = 1$ on the right hand side of the x axis, is highly efficient and 94% of the traveling signals succeed in reaching the target for a time-out value of $t = 1000$, with an average stretch of 9. Yet not all paths are successful within the given time-out, such that the success rate is not strictly 1. This situation is much worse for the weight-biased random walk at the other extreme of the spectrum of routing strategies, represented at the left hand side of the x axis around $\lambda = 0$. Here, only 42% of the signals reach successfully the target for a time-out of $t = 1000$, and they do it with an average stretch of 169. Only when

[1] We also explored another framework in which we considered as spatial information the total distance from the current node to the target while traveling through neighbor j, $d^{\mathrm{E}} = d^{\mathrm{E}}_{ij} + d^{\mathrm{E}}_{jz}$. The results obtained were qualitatively similar to the ones procured using Eq. (8), see Fig. SF47, but using only d^{E}_{jz} allows for easier comparison with standard greedy routing.

[2] In order to assess to which extent the outcome varies across realizations, we calculated 100 instances with different seeds of the navigation protocols in the λ-spectrum for subject 0 in the UL dataset and time-outs 1000 and 10 000. We found that the coefficient of variation between realizations is $c_v \simeq 10^{-3}$, see SF10. Consequently, and given that we focus on the average outcome of the dataset, running only one realization per subject for each time-out does not introduce any substantial bias to the results.

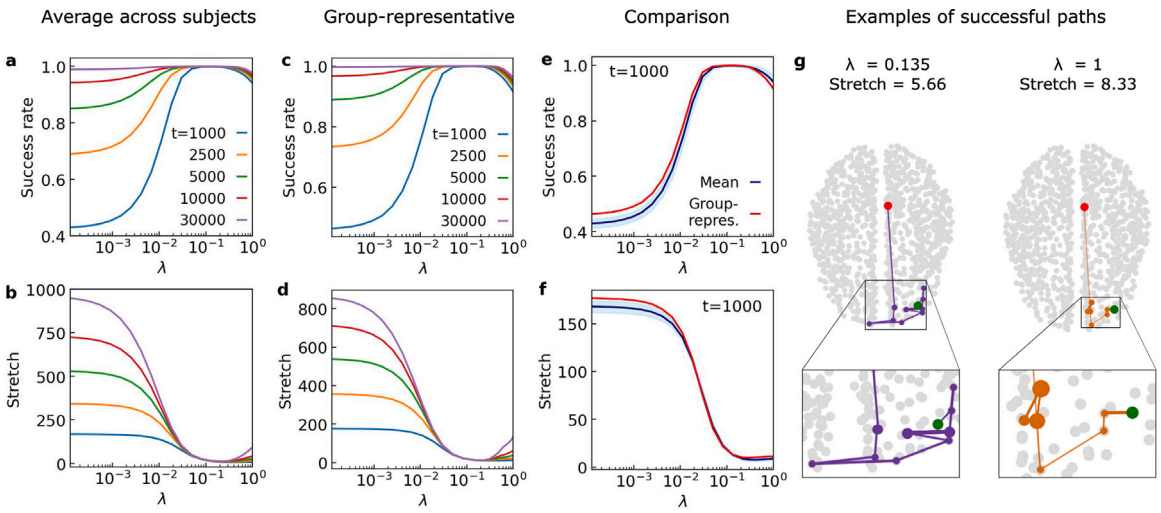

Fig. 3. Navigation results. (a) Mean success rate and (b) mean average stretch across the 40 subjects in the UL Dataset. Each curve shows the outcome for a specific value of time-out. (c) Success rate and (d) stretch for the navigation of the group-representative connectome for different values of time-out. (e) and (f) for t = 1000, comparison of the success rate/average stretch for the group-representative connectome (in red) and the mean success rate/average stretch of all subjects (in blue). The blue-shadowed area corresponds to two times the standard deviation between subjects. (g) Path taken from ROI 154 to ROI 20 of the group-representative connectome for $\lambda = 0.135$ – sweet-spot region – (in purple), and $\lambda = 1$ (in orange). The source node is represented in red, the target node in green. In the insets below, the size of the colored nodes is proportional to the number of times the signal visits them.

Table 1
λ value at the center of the sweet spot domain and its standard deviation across subjects in the UL dataset for the five time-outs studied. The third column shows the relative contributions to the transmission probability of the mean average spatial distance between all pairs of ROIs, $\langle d_E \rangle = 74$ mm, and the mean average weight distance between connected ROIs, $\langle d_w \rangle = 6.8$ mm.

Time-out	λ	$[\langle d_E \rangle \cdot \lambda]/[\langle d_w \rangle \cdot (1-\lambda)]$
1000	0.129 ± 0.018	1.61
2500	0.12 ± 0.04	1.48
5000	0.10 ± 0.04	1.21
10 000	0.08 ± 0.04	0.94
30 000	0.07 ± 0.04	0.82

the time-out is further increased, the success rate grows at the expense of an even larger stretch, implying an extremely lengthy transmission time.

More importantly, the experiments reveal that regardless of the time-out there exists a domain of λ values around 0.1 where the success rate is maximum, and more than 99% of the traveling signals reach the target. Interestingly, in this domain of λ the average stretch reaches a minimum, with a value of 8 for $t = 1000$. The transmission costs also have a minimum in the same λ domain, see Fig. SF8. This means that guiding the routing process with a combination of weights and spatial distances results in optimal navigability. The same behavior was obtained using the HCP dataset, although the maximum, and specially the minima, are less pronounced. In this dataset, the λ value at the center of the domain switches slightly to the left, around $\lambda \simeq 0.08$, see Fig. SF55.

4.3. Sweet spot of optimal navigability

Table 1 shows the average over all subjects in the UL dataset of the λ value at the center of the sweet spot for each time-out. The λ at the center of the sweet spot for each individual subject was selected as the value with the highest success rate among the 25 different values of λ for which we had run the simulations. We note that the values presented in Table 1 are the center of a wider domain of λ values for which the navigation is optimal.

As the time-out decreases below $t = 1000$, the optimal navigability domain gradually evolves into a single maximum of the success rate with decreasing height at values of λ progressively closer to $\lambda = 1$, see Fig. SF9. As we have previously seen, for $\lambda \geq 1000$, the optimal performance occurs in a plateau of values around $\lambda \simeq 0.1$. In the optimal domain, spatial and weight distances are balanced and therefore approximately equally relevant, meaning that their relative contribution to the transmission probability is of the same order of magnitude. To quantify this balance, the relative importance between the spatial and the weight average distances at the center of the optimal λ domain ($\lambda \simeq 0.1$) can be calculated as $(74 \cdot \lambda)/(6.8 \cdot (1-\lambda)) \simeq 1.21$, where 74 ± 3 mm is the mean average spatial distance between all pairs of ROIs across subjects in the UL dataset and 6.80 ± 0.12 mm is the mean value of the average weight distance between connected ROIs, see Figs. SF20–SF22. Table 1 provides the specific ratios for the different time-outs. For the UL group-representative connectome, this ratio is almost identical, of $(73.8 \cdot 0.1)/(6.83 \cdot 0.9) \simeq 1.2$.

It is important to highlight that all navigation magnitudes are accurately described by the group-representative for all time-outs, Fig. 3c, d and SF14. Specially, the maximum navigability region is well reproduced in the group-representative connectome, with outcomes that are very similar to the mean of all subjects. Fig. 3e and f show the comparison of the UL group-representative outcome and the mean results of the dataset for $t = 1000$, while Figs. SF15–SF19 show the results for all time-out values. In these figures we can see that, as the time-out increases, the group-representative slightly departs from the mean of all subjects.

In Fig. 3g we show an example of two successful paths taken to transmit a signal from ROI 154 to ROI 20 in the group-representative connectome for $\lambda = 0.135$ (within the range of optimal λ) and $\lambda = 1$. This example illustrates the advantage of incorporating both weights and spatial distances when navigating the network rather than solely considering the latter. In the zoomed area shown at the bottom, the colored ROI's sizes are directly proportional to the number of times the signal reaches them. The increased sizes for $\lambda = 1$ indicate that, when only considering spatial distances, the signal gets stuck for a long time between three of the nodes in the path until it can finally escape.

Regarding the HCP dataset, the relative importance between spatial and weight distances at the center of its optimal λ domain ($\lambda \simeq 0.08$) is $(74 \cdot 0.08)/(9 \cdot 0.92) \simeq 0.72$, and for its group-representative $(73.7 \cdot 0.08)/(9 \cdot 0.92) \simeq 0.71$. Figures SF55 and SF57–SF62 display the average navigation results for the subjects in this dataset and the comparison with the results of its group-representative. Also in this dataset, all navigation magnitudes are accurately described by the group-representative

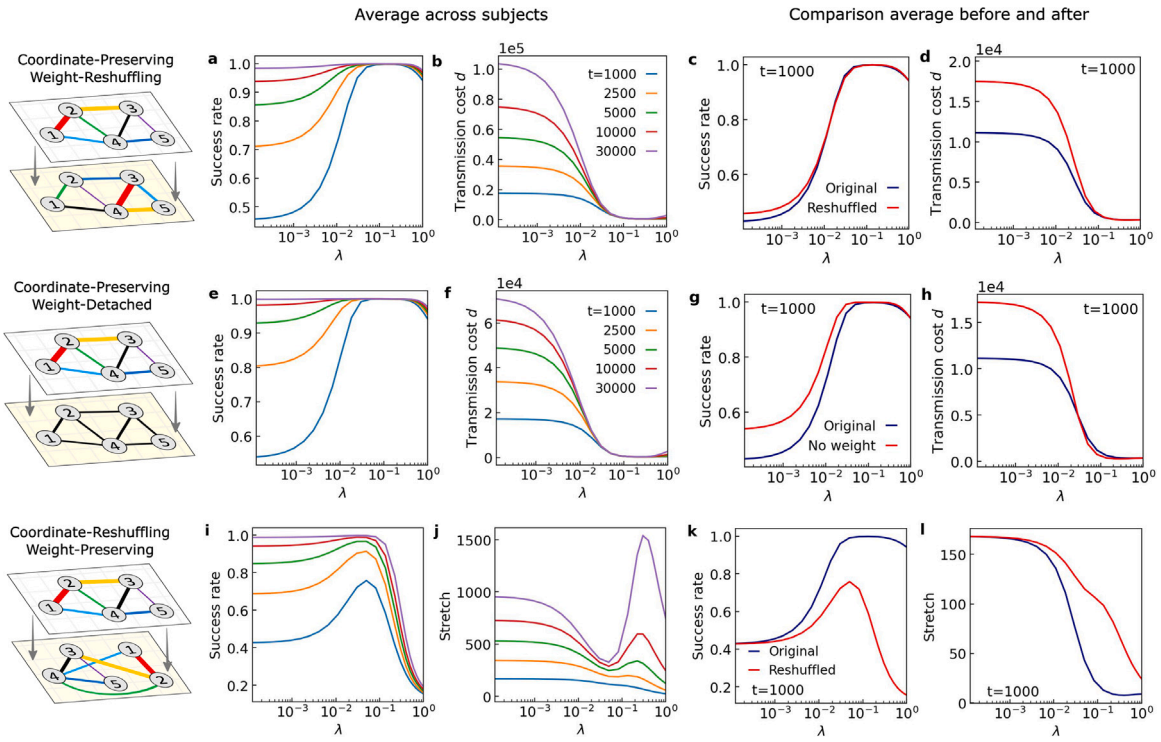

Fig. 4. Top row: Navigation after Coordinate-Preserving Weight-Reshuffling. (a) Average success rate and (b) average spatial distance transmission cost for the weight-reshuffled surrogates of the 40 subjects in the UL dataset and different values of the time-out. Comparison of (c) the success rate and (d) the spatial distance transmission cost of the original networks and weight-reshuffled surrogates for t = 1000. **Middle row: Navigation after Coordinate-Preserving Weight-Detached.** The same as in (a)–(d) in surrogates with constant weights. **Bottom row: Navigation after Coordinate-Reshuffling Weight-Preserving.** The same as in (a)–(d) but with stretch instead of spatial distance transmission cost, in surrogates where the spatial coordinates of the different ROIs have been reshuffled.

and the slight discrepancy between the mean results of all individuals and the ones for the group-representative grows with the time-out.

4.4. Assessing the role of weights in maximum navigability

To understand the contribution of weights and spatial distances to HWSD navigability, we compared the results for real connectomes with routing experiments in three types of surrogate connectomes, where the inverse relationship between weights and distances observed in the real networks was disrupted by randomizing some structural features. Since the results can vary depending on the specific realization of the randomization, we performed the navigation for $t = 5000$ on 50 different randomizations for the same subject, and we found that there is little variation between them, with a maximum coefficient of variation $c_v \simeq 7\times10^{-2}$, Figs. SF29 and SF42. Given that we focus on the qualitative differences between null models and original networks, and we are already averaging over subjects, we only ran one realization per subject for each time-out.

***Coordinate-Preserving Weight-Reshuffling* (CP-WR) null model.** The average of the navigation performance metrics for CP-WR surrogates of the individual subjects in the UL dataset are shown in Fig. 4a, b and SF23. The comparison of the original results and the results for the CP-WR surrogates are shown in Fig. 4c and d. The success rate, the average stretch, and the transmission cost of weight distances are maintained for all values of λ. In particular, the optimal navigability domain is not disrupted. By contrast, the difference in the transmission cost of spatial distances between the original connectomes and the randomized surrogates increases as λ decreases. In the original connectome, when the navigation protocol prioritizes traveling through connections with high weights, neighbors that are close in space are selected. The reshuffling of weights disrupts this correlation and, consequently, the signals traverse a longer total distance in the reshuffled network than in the original one. Finally, the pattern of the outcomes is qualitatively similar for the various time-outs studied in this work, Figs. SF24–SF28.

***Coordinate-Preserving Weight-Detached* (CP-WD) null model.** In addition, we tested the behavior when weights are constant, meaning that the contribution of the weight distances to the transmission probability is always the same independently of the connection. As a result, the transmission probability can be rewritten as $P_\lambda(j\ |i,z) = \exp\left[-(\lambda\cdot d^{\mathrm{E}}_{jz})\right]\frac{1}{\tilde{Z}^z}$, where $\tilde{Z}^z = \sum_j \exp\left[-(\lambda\cdot d^{\mathrm{E}}_{jz})\right]$ is the normalization factor. Notice that the transmission probability becomes effectively independent of the weight distance due to the full homogeneity of weights, but their influence in the navigation process is still there and controlled by the value of λ, which rescales the spatial distance. As a result, the routing protocol interpolates between the dynamics of an unbiased random walk at $\lambda = 0$, where all the probabilities to arrive to neighboring regions have the same value, and a pure stochastic greedy routing at the $\lambda = 1$ extreme of the spectrum.[3] Experiments on CP-WD surrogates show that, as in CP-WR, the optimal navigability domain is not disrupted but the transmission cost of spatial distances between the original connectomes and the randomized surrogates increases as λ decreases, see Fig. 4e–h and SF30–SF35. In addition, in these surrogates we observe a slight improvement in the success rate and average stretch for low values of λ.

We obtained similar results when we assigned the weight distances at random from a uniform distribution around the mean.

***Coordinate-Reshuffling Weight-Preserving (CR-WP)* null model.** In CR-WP surrogates, the navigation guided by spacial distances procured worse results than the weight-biased random walk, see Fig. 4i, j and SF36. Precisely, the amount of successful paths for $\lambda = 1$ was below 20%. Even when coordinates are reshuffled, there is a range of λ values (close to the sweet spot in the original connectomes) for which

[3] Deterministic greedy routing is recovered for $\lambda \to \infty$.

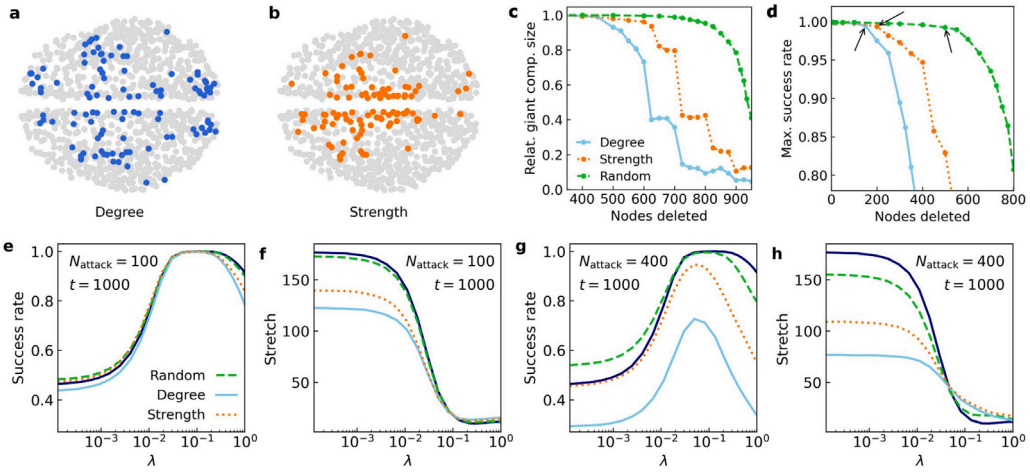

Fig. 5. Effects of attacks on the UL group-representative connectome. (a) ROIs deleted in the targeted attack on nodes with highest degree and (b) with highest strength for $N_{attack} = 100$. (c) Evolution of the relative size of the giant connected component of the network as nodes are deleted. (d) Evolution of the maximum success rate reached as a function of the nodes deleted. The arrows point at each of the points where the success rate does not reach anymore the value it had in the sweet spot for the original network. (e, g) Success rate and (f, h) average stretch after deleting 100 and 400 nodes of the network, respectively. The dark-blue curve represents the original results, the dashed green line the results after deleting nodes at random, the light blue plain curve corresponds to the targeted attack on nodes with highest degree and the dotted orange curve to the attack on nodes with highest strength.

the success rate still has a maximum, although it does not reach the level of the sweet spot. Therefore, complementing the weight-biased random walk with information about spatial distances improves the performance of the routing protocol due to an increased chance of traveling through small-weight connections. This diversifies the choice of neighbors as compared to the bare weight-biased random walk, increasing the capacity of reaching more targets within the time-out. At larger values of λ, the stochastic greedy routing based on spatial distances dominates, and the fact that distances are not coupled to the topology causes the success rate to drop steadily. The comparison of the averages of all measures before and after the reshuffling, Fig. 4k, l and SF37–SF41, shows that the CR-WP randomization leads to a performance decline in all magnitudes.

4.5. Maximum navigability is resilient under targeted attack

Finally, we evaluated the resilience of the navigability using the HWSD routing protocol for $t = 1000$ in the group-representative connectome. With this purpose, we inflicted a targeted attack on the ROIs with highest degree (HD), Fig. 5a, and on the ROIs with highest strength (HS), Fig. 5b. As a baseline reference, we simulated random failure of the system.

As expected, the differences between the navigation of the original networks and of the perturbed ones increase as the number of attacked regions grows, regardless of the type of attack. Also, the targeted attacks are not able to disconnect the remaining ROIs, which typically form a robust giant connected component. For instance, it is necessary to remove approximately 45% of the ROIs in decreasing order of degree to break off the connectome. This percentage rises to 60% in descending order of strength, and to 80% when nodes are deleted at random, see Fig. 5c.

Fig. 5e–h display the results for $N_{attack} = 100, 400$. Even after removing 10% of the ROIs, i.e. 100 nodes, the success rate maintains the original performance and the existence of the maximum navigability sweet spot. For this amount of nodes deleted, the three types of damage produce very similar results to the original network. In fact, the navigation after random attack behaves similarly as in the unperturbed network even after the deletion of 400 nodes. However, the HD and HS perturbations affect more strongly the navigability of the connectomes, and after the removal of 400 nodes all magnitudes are severely disrupted. In Figs. SF43 and SF44 we show the results for HD and HS after the deletion of different number of nodes. For both attacks, the success rate decreases for most values of λ as we progressively delete nodes, but HS has a smaller effect than HD. The average stretch has two different behaviors on each side of the minimum: to the right it approximately remains without changes, and to the left it slightly improves as nodes are deleted. The spatial distances transmission cost has a behavior similar to the stretch, and the weight distances transmission cost worsens for all values of λ as the number of deleted nodes increases.

It is interesting to notice that none of the attacks affect significantly the efficiency of the HWSD protocol in the optimal navigability domain. Even after the removal of the top 15% of nodes with highest degree, 20% of nodes with highest strength and 50% at random, there is a region in the spectrum of λ where navigation is still optimal, see Fig. 5d and SF43–SF45. In other words, even after serious damage, guiding navigation by combining weights and distances ensures that signals can be delivered to almost every ROI remaining in the connectome.

5. Discussion and conclusions

The findings reported in this work are qualitatively similar at the personalized level for all subjects in the UL and HCP datasets and for their group-representatives, despite the discrepancy in their average connectivity. In all cases, weights facilitate a sweet spot in which communication is fully amplified with low costs. Remarkably, the phenomenon is resilient, and optimal navigability is achieved even under serious damage. Then, communication in the brain is not only affected by its large-scale architecture (and in particular by its small-world property resulting from short topological distances) but also by the dynamic rules involved in the transmission process. More specifically, the existence of a short topological path between two nodes does not ensure that a stochastic routing protocol, which selects at random the next neighbor to visit according to some probability, is able to find the shortest path in a short time. What is certain is that stochastic routing protocols reach a full success rate with all signals reaching eventually the target. As a counterpoint, some signals could take an exceedingly lengthy time.

In fact, the biological implausibility of the exceedingly lengthy transmission times found in the pure weight-biased random walk is an indication that it is not a biologically rational choice for routing information in brain connectomes. In the protocol proposed here, a signal is selectively transmitted to an area of the brain by combining the information of link weights and spatial distances, in contrast with

previous works where only one or another was taken into account but not both simultaneously. As a result, the HWSD routing strategy leads to an optimal combination that is not unique, there exists a range of values calibrating the participation of the weights in the greedy routing that produces a sweet spot in which the success rate is maximal with minimum transmissibility cost, even for decreased time-outs.

These results support the claim that effective communication in the brain is sustained not only by its *hard wiring* – the topology and geometric layout – but also by its *soft wiring*—the intensities of the connections. The brain, and the nervous system in general, is plastic and has the ability to adapt to external or internal changes by reorganizing its structure and functions. Apart from extreme events, for instance injuries such as stroke, the reshaping of neural connections and their strength can also be induced by processes such as memory storage and learning (Pascual-Leone et al., 2005). Not all the reconfiguration processes have the same cost or occur at the same time scale. Changes in the *hard wiring* of the brain, that is, the large scale connectivity structure of the connectome, are rare and can only happen to a very limited extent. In contrast, changes in the *soft wiring*, understood as a reconfiguration of weights such that new knowledge or experiences are fixed, are an everyday process.

Disturbing the specific form in which weights are arranged in the connectomes or the variability of their values do not compromise the optimal navigability phenomenon either. This result is congruent with the hypothesis that efficient communication between brain regions (Laughlin and Sejnowski, 2003), needed to support ultrafast responses of the brain to external and internal stimuli and ultimately sustain behavior and cognition, should not depend crucially on memory or learning processes that can dynamically change the configuration of weights at short time scales. Even if the navigation success is not affected by the specific configuration of weights in the connectomes, we found that it contributes to optimal navigability by decreasing the spatial distance transmission cost. Specifically, the inverse correlation between weights and distances, which can be explained by an economy principle related with longer connections requiring more resources, facilitates signals to travel a shorter spatial distance to reach the target.

The maximum in the navigability could be interpreted as a stochastic resonance effect (Wellens et al., 2003; Calim et al., 2021), where the choice of transmission paths is more varied as compared to pure stochastic greedy routing, and in which new efficient routes can be found. In our work, weights play the constructive role of noise to achieve optimal navigability. Interestingly, other investigations have found other stochastic resonance effects in the human brain (Faisal et al., 2008). It was found that non-zero levels of noise enhance information transmission in a dynamic model of the human cortex connectome, inducing a stochastic resonance effect when the system is in a critical regime (Vázquez-Rodríguez et al., 2017). Another example is the noise added by transcranial magnetic stimulation, which is able to induce a stochastic resonance effect that may explain why parameters that under normal circumstances impair behavior can induce behavioral facilitations (Schwarzkopf et al., 2011).

Communication processes in the brain may be ruled by different dynamical mechanisms depending on the resolution scale, from microscale neurons to macroscale region levels. At the macroscale of higher brain areas treated in our work, there is evidence of selective information routing. It has been observed (Ciocchi et al., 2015) that ventral hippocampal neurons route anxiety-related information preferentially to the prefrontal cortex and goal-related information preferentially to the nucleus accumbens. These results prove that higher cortical areas do not communicate by transmitting the signals equally but by routing the information according to content and target, which is consistent with the targeting-directed principle guiding greedy routing. Yet many questions remain for future work. For instance, to discern the role of the economy principle in guiding selective information transmission through intermediate areas, and whether it favors those areas closer to the target. On a different level, other open questions are the developmental and evolutionary processes that control the specific spatial positioning of brain regions, the relation between specific configurations of weights in connectome links and different brain states, functional responses and learning-memory processes, as well as the impact of damage or specific diseases on brain navigability.

Ethics statement

For this work, we used previously published datasets. The studies to obtain the UL dataset were reviewed and approved by the University of Lausanne (protocol approved by the Ethics Committee of Canton de Vaud (CERV-VD)). The studies to obtain the HCP dataset were reviewed and approved by the Human Connectome Project. All participants provided their written informed consent to participate in the respective study.

CRediT authorship contribution statement

Laia Barjuan: Writing – review & editing, Visualization, Validation, Software, Investigation, Formal analysis. **Jordi Soriano:** Writing – review & editing, Investigation, Funding acquisition, Formal analysis. **M. Ángeles Serrano:** Writing – review & editing, Writing – original draft, Validation, Supervision, Methodology, Investigation, Funding acquisition, Formal analysis, Conceptualization.

Declaration of competing interest

The authors declare no competing interests.

Data availability

The UL and HCP weighted human connectomes are available via the Zenodo platform at https://doi.org/10.5281/zenodo.11198345. Our source codes will be available upon publication via the GitHub platform at https://github.com/networkgeometry.

Acknowledgments

We thank Patric Hagmann and Yasser Alemán Gómez for sharing the data, and Marián Boguñá for helpful comments. L.B. acknowledges support from an FPU21/03183 grant by the Spanish Ministry of Science, Innovation and Universities, and from "la Caixa" Foundation (ID 100010434) under the agreement LCF/PR/HR19/52160007. J.S. acknowledges support from grant PID2022-137713NB-C22, funded by MCIU/AEI/10.13039/501100011033 and by ERDF/EU, and by the Generalitat de Catalunya under grant 2021-SGR-00450. M.A.S. acknowledges support from grants PID2019-106290GB-C22 and PID2022-137505NB-C22 funded by MCIU/AEI/10.13039/501100011033 and by ERDF/EU, and from grant number 2021-SGR-00856 by the Generalitat de Catalunya.

Appendix A. Supplementary data

Supplementary material related to this article can be found online at https://doi.org/10.1016/j.neuroimage.2024.120703.

References

Allard, A., Serrano, M.Á., 2020. Navigable maps of structural brain networks across species. PLoS Comput. Biol. 16 (2), 1–20.

Avena-Koenigsberger, A., Kolchinsky, A., Yan, X., van den Heuvel, M.P., Hagmann, P., Sporns, O., 2019. A spectrum of routing strategies for brain networks. PLoS Comput. Biol. 15 (3), e1006833.

Avena-Koenigsberger, A., Mišić, B., Hawkins, R.X.D., et al., 2017. Path ensembles and a tradeoff between communication efficiency and resilience in the human connectome. Brain Struct. Funct. 222, 603–618.
Avena-Koenigsberger, Andrea, Misic, Bratislav, Sporns, Olaf, 2018. Communication dynamics in complex brain networks. Nat. Rev. Neurosci. 19 (1), 17–33.
Bassett, Danielle Smith, Bullmore, E.D., 2006. Small-world brain networks. Neurosci. 12 (6), 512–523.
Bassett, Danielle S., Bullmore, Edward T., 2017. Small-world brain networks revisited. Neurosci. 23 (5), 499–516.
Betzel, Richard F., Griffa, Alessandra, Hagmann, Patric, Mišić, Bratislav, 2019. Distance-dependent consensus thresholds for generating group-representative structural brain networks. Netw. Neurosci. 3 (2), 475–496.
Bressler, Steven L., Menon, Vinod, 2010. Large-scale brain networks in cognition: emerging methods and principles. Trends in Cognitive Sciences 14 (6), 277–290.
Bullmore, Ed., Sporns, Olaf, 2012. The economy of brain network organization. Nat. Rev. Neurosci. 13 (5), 336–349.
Calim, Ali, Palabas, Tugba, Uzuntarla, Muhammet, 2021. Stochastic and vibrational resonance in complex networks of neurons. Phil. Trans. R. Soc. A 379 (2198), 20200236.
Cammoun, Leila, Gigandet, Xavier, Meskaldji, Djalel, Thiran, Jean Philippe, Sporns, Olaf, Do, Kim Q., Maeder, Philippe, Meuli, Reto, Hagmann, Patric, 2012. Mapping the human connectome at multiple scales with diffusion spectrum mri. J. Neurosci. Methods 203 (2), 386–397.
Cannistraci, Carlo Vittorio, Muscoloni, Alessandro, 2022. Geometrical congruence, greedy navigability and myopic transfer in complex networks and brain connectomes. Nature Commun. 13 (1), 7308.
Ciocchi, S., Passecker, J., Malagon-Vina, H., Mikus, N., Klausberger, T., 2015. Selective information routing by ventral hippocampal ca1 projection neurons. Science 348 (6234), 560–563.
Deco, Gustavo, Kringelbach, Morten L., 2014. Great expectations: using whole-brain computational connectomics for understanding neuropsychiatric disorders. Neuron 84 (5), 892–905.
Ercsey-Ravasz, Mária, Markov, Nikola T., Lamy, Camille, Van Essen, David C., Knoblauch, Kenneth, Toroczkai, Zoltán, Kennedy, Henry, 2013. A predictive network model of cerebral cortical connectivity based on a distance rule. Neuron 80 (1), 184–197.
Faisal, A. Aldo, Selen, Luc P.J., Wolpert, Daniel M., 2008. Noise in the nervous system. Nat. Rev. Neurosci. 9 (4), 292–303.
Garyfallidis, Eleftherios, Brett, Matthew, Amirbekian, Bagrat, Rokem, Ariel, Walt, Stefan Van Der, Descoteaux, Maxime, Nimmo-Smith, Ian, Dipy Contributors, 2014. Dipy, a library for the analysis of diffusion mri data. Front. Neuroinform. 8, 8.
Gastner, Michael T., Ódor, Géza, 2016. The topology of large open connectome networks for the human brain. Sci. Rep. 6 (1), 27249.
Glasser, Matthew F., Sotiropoulos, Stamatios N., Wilson, J. Anthony, Coalson, Timothy S., Fischl, Bruce, Andersson, Jesper L., Xu, Junqian, Jbabdi, Saad, Webster, Matthew, Polimeni, Jonathan R., et al., 2013. The minimal preprocessing pipelines for the human connectome project. Neuroimage 80, 105–124.
Gong, Gaolang, He, Yong, Concha, Luis, Lebel, Catherine, Gross, Donald W., Evans, Alan C., Beaulieu, Christian, 2009. Mapping anatomical connectivity patterns of human cerebral cortex using in vivo diffusion tensor imaging tractography. Cerebral Cortex 19 (3), 524–536.
Goñi, Joaquín, van den Heuvel, Martijn P., Avena-Koenigsberger, Andrea, de Mendizabal, Nieves Velez, Betzel, Richard F., Griffa, Alessandra, Hagmann, Patric, Corominas-Murtra, Bernat, Thiran, Jean-Philippe, Sporns, Olaf, 2014. Resting-brain functional connectivity predicted by analytic measures of network communication. Proc. Natl. Acad. Sci. 111 (2), 833–838.
Hagmann, Patric, Kurant, Maciej, Gigandet, Xavier, Thiran, Patrick, Wedeen, Van J., Meuli, Reto, Thiran, Jean-Philippe, 2007. Mapping human whole-brain structural networks with diffusion mri. PLoS One 2 (7), e597.
He, Yong, Chen, Zhang J., Evans, Alan C., 2007. Small-world anatomical networks in the human brain revealed by cortical thickness from mri. Cerebral Cortex 17 (10), 2407–2419.
Honey, Christopher J., Kötter, Rolf, Breakspear, Michael, Sporns, Olaf, 2007. Network structure of cerebral cortex shapes functional connectivity on multiple time scales. Proc. Natl. Acad. Sci. 104 (24), 10240–10245.
Kleinberg, Jon M., 2000. Navigation in a small world. Nature 406 (6798), 845.
Laughlin, Simon B., Sejnowski, Terrence J., 2003. Communication in neuronal networks. Science 301 (5641), 1870–1874.
Meunier, David, Lambiotte, Renaud, Bullmore, Edward T., 2010. Modular and hierarchically modular organization of brain networks. Front. Neurosci. 4, 200.
Mišić, Bratislav, Betzel, Richard F., Nematzadeh, Azadeh, Goni, Joaquin, Griffa, Alessandra, Hagmann, Patric, Flammini, Alessandro, Ahn, Yong-Yeol, Sporns, Olaf, 2015. Cooperative and competitive spreading dynamics on the human connectome. Neuron 86 (6), 1518–1529.
Ortiz, Elisenda, Starnini, Michele, Serrano, M. Ángeles, 2017. Navigability of temporal networks in hyperbolic space. Sci. Rep. 7 (1), 15054.
Pascual-Leone, Alvaro, Amedi, Amir, Fregni, Felipe, Merabet, Lotfi B., 2005. The plastic human brain cortex. Annu. Rev. Neurosci. 28, 377–401.
Schwartz, Ernst, Nenning, Karl-Heinz, Heuer, Katja, Jeffery, Nathan, Bertrand, Ornella C., Toro, Roberto, Kasprian, Gregor, Prayer, Daniela, Langs, Georg, 2023. Evolution of cortical geometry and its link to function, behaviour and ecology. Nature Commun. 14 (1), 2252.
Schwarzkopf, Dietrich Samuel, Silvanto, Juha, Rees, Geraint, 2011. Stochastic resonance effects reveal the neural mechanisms of transcranial magnetic stimulation. J. Neurosci. 31 (9), 3143–3147.
Seguin, C., van den Heuvel, M.P., Zalesky, A., 2018. Navigation of brain networks. Proc. Natl. Acad. Sci. USA 115, 6297–6302.
Seguin, Caio, Sporns, Olaf, Zalesky, Andrew, 2023. Brain network communication: concepts, models and applications. Nat. Rev. Neurosci. 24, 557–574.
Serrano, M. Ángeles, Boguñá, Marián, Vespignani, Alessandro, 2009. Extracting the multiscale backbone of complex weighted networks. Proc. Natl. Acad. Sci. 106 (16), 6483–6488.
Sporns, Olaf, Betzel, Richard F., 2016. Modular brain networks. Annu. Rev. Psychol. 67, 613–640.
Sporns, Olaf, Chialvo, Dante R., Kaiser, Marcus, Hilgetag, Claus C., 2004. Organization, development and function of complex brain networks. Trends in Cognitive Sciences 8 (9), 418–425.
Sporns, Olaf, Tononi, Giulio, Kötter, Rolf, 2005. The human connectome: a structural description of the human brain. PLoS Comput. Biol. 1 (4), e42.
Stiso, Jennifer, Bassett, Danielle S., 2018. Spatial embedding imposes constraints on neuronal network architectures. Trends in Cognitive Sciences 22 (12), 1127–1142.
Tourbier, Sebastien, Aleman-Gomez, Yasser, Mullier, Emeline, Griffa, Alessandra, Cuadra, Meritxell Bach, Hagmann, Patric, 2020. connectomic-slab/connectomemapper3: Connectome Mapper v3.0.0-beta-RC1. Funded by Sinergia Grant 170873 from the Swiss National Science Foundation (See http://p3.snf.ch/Project-170873 for details).
Tournier, J-Donald, Calamante, Fernando, Connelly, Alan, 2007. Robust determination of the fibre orientation distribution in diffusion mri: non-negativity constrained super-resolved spherical deconvolution. Neuroimage 35 (4), 1459–1472.
Tournier, J.-Donald, Calamante, Fernando, Connelly, Alan, 2012. Mrtrix: diffusion tractography in crossing fiber regions. Int. J. Imaging Syst. Technol. 22 (1), 53–66.
Van Den Heuvel, Martijn P., Sporns, Olaf, 2011. Rich-club organization of the human connectome. J. Neurosci. 31 (44), 15775–15786.
Van Essen, D.C., Ugurbil, K., Auerbach, E., Barch, D., Behrens, T.E.J., Bucholz, R., Chang, A., Chen, L., Corbetta, M., Curtiss, S.W., Della Penna, S., Feinberg, D., Glasser, M.F., Harel, N., Heath, A.C., Larson-Prior, L., Marcus, D., Michalareas, G., Moeller, S., Oostenveld, R., Petersen, S.E., Prior, F., Schlaggar, B.L., Smith, S.M., Snyder, A.Z., Xu, J., Yacoub, E., 2012. The human connectome project: a data acquisition perspective. Neuroimage 62 (4), 2222–2231.
Vázquez-Rodríguez, B., Avena-Koenigsberger, A., Sporns, O., et al., 2017. Stochastic resonance at criticality in a network model of the human cortex.
Watts, Duncan J., Strogatz, Steven H., 1998. Collective dynamics of 'small-world'networks. Nature 393 (6684), 440–442.
Wellens, Thomas, Shatokhin, Vyacheslav, Buchleitner, Andreas, 2003. Stochastic resonance. Rep. Progr. Phys. 67 (1), 45.